

Structure of the calcium dependent type 2 secretion pseudopilus

Aracelys Lopez-Castilla, Jenny-Lee Thomassin, Benjamin Bardiaux, Weili Zheng, Mangayarkarasi Nivaskumar, Xiong Yu, Michael Nilges, Edward Egelman, Nadia Izadi-Pruneyre, Olivera Francetic

▶ **To cite this version:**

Aracelys Lopez-Castilla, Jenny-Lee Thomassin, Benjamin Bardiaux, Weili Zheng, Mangayarkarasi Nivaskumar, et al.. Structure of the calcium dependent type 2 secretion pseudopilus. Nature Microbiology, 2017, 10.1038/s41564-017-0041-2 . pasteur-02283219

HAL Id: pasteur-02283219
https://pasteur.hal.science/pasteur-02283219

Submitted on 10 Sep 2019

HAL is a multi-disciplinary open access archive for the deposit and dissemination of scientific research documents, whether they are published or not. The documents may come from teaching and research institutions in France or abroad, or from public or private research centers.

L'archive ouverte pluridisciplinaire **HAL**, est destinée au dépôt et à la diffusion de documents scientifiques de niveau recherche, publiés ou non, émanant des établissements d'enseignement et de recherche français ou étrangers, des laboratoires publics ou privés.



Distributed under a Creative Commons Attribution - NonCommercial - ShareAlike 4.0 International License

Structure of the calcium dependent type 2 secretion pseudopilus

Aracelys Lopez-Castilla[1,5], Jenny-Lee Thomassin[2,5], Benjamin Bardiaux[3,5], Weili Zheng[4], Mangayarkarasi Nivaskumar[2], Xiong Yu[4], Michael Nilges[3], Edward H. Egelman[4], Nadia Izadi-Pruneyre[1*], Olivera Francetic[2*]

[1]NMR of Biomolecules Unit, Department of Structural Biology and Chemistry, Institut Pasteur, CNRS UMR3528, 28 rue du Dr Roux, 75724 Paris, France

[2]Biochemistry of Macromolecular Interactions Unit, Department of Structural Biology and Chemistry, Institut Pasteur, CNRS ERL6002, 28 rue du Dr Roux, 75724 Paris, France.

[3]Structural Bioinformatics Unit, Department of Structural Biology and Chemistry, CNRS UMR3528, Institut Pasteur, 25 rue du Dr Roux, 75724 Paris, France

[4]Department of Biochemistry and Molecular Genetics, University of Virginia, Charlottesville, VA22908, USA

[5]Equal contribution.

[*]Corresponding authors.

Keywords: type 2 secretion system, solution NMR, cryoEM, calcium, protein folding, type 4 filaments

Abstract

Many Gram-negative bacteria use type 2 secretion systems (T2SS) to secrete proteins involved in virulence and adaptation. Transport of folded proteins *via* T2SS nanomachines requires the assembly of inner membrane-anchored fibers called pseudopili. Although efficient pseudopilus assembly is essential for protein secretion, structure-based functional analyses are required to unravel the mechanistic link between these processes. Here, we report an atomic model for a T2SS pseudopilus from *Klebsiella oxytoca*, obtained by fitting the NMR structure of its calcium-bound subunit PulG into the ~ 5 Å resolution cryo-electron microscopy (cryoEM) reconstruction of assembled fibers. This structure reveals the comprehensive network of inter-subunit contacts and unexpected features, including a disordered central region of the PulG helical stem, and highly flexible C-terminal residues on the fiber surface. NMR, mutagenesis and functional analyses highlight the key role of calcium in PulG folding and stability. Fiber disassembly in the absence of calcium provides a basis for pseudopilus length control, essential for protein secretion, and supports the Archimedes' screw model for T2S mechanism.

Main text

Microorganisms profoundly transform their environment by colonizing biotic and abiotic surfaces and assimilating nutrients from organic and mineral sources. In many prokaryotes, nanomachines of the type 4 filament (Tff) superfamily[1] mediate adaptive functions by promoting cell adhesion, motility and macromolecular transport. The Tff assembly systems, including archaeal flagella[2], bacterial type 4 pili (T4P) and T2SSs[3], use a conserved mechanism to polymerise fibres from protein subunits initially localised in the plasma membrane. In Gram-negative bacteria T2SSs promote assembly of periplasmic fibres called

pseudopili to drive secretion of specific folded proteins, including macromolecule hydrolases, toxins, adhesins or cytochromes with key roles in virulence and niche survival[4].

T2SSs are large trans-envelope nanomachines that coordinate the activity of a cytoplasmic ATPase and inner membrane assembly sub-complex to polymerize pseudopilin subunits into helical fibres (Fig. 1a). Pseudopili are composed mainly of major pseudopilin, called PulG in the prototypical *Klebsiella oxytoca* pullulanase T2SS[5]. Four minor pseudopilins PulH, I, J and K, likely cap the pseudopilus tip and promote efficient initiation of fibre assembly[6,7]. Pseudopilus assembly is coupled to secretion of folded proteins from the periplasm across the dedicated outer membrane channel to the extracellular milieu[8], however the mechanism of this coupling remains unknown.

Structural information is essential to understand the secretion process at molecular and atomic levels. The first crystal structure of the major pseudopilin PulG from *K. oxytoca* T2SS showed a typical α-β pilin fold in a crystallographic dimer where the C-terminal β strand was swapped between two monomers[9]. Subsequent crystallographic studies of PulG homologues from *Vibrio cholerae, V. vulnificus* and enterohaemorrhagic *Escherichia coli* revealed local structural differences at the C-terminus including a long loop harbouring a calcium atom[10]. Substitutions of two calcium-coordinating residues in the *V. cholerae* pseudopilin EpsG abolished protein secretion[10], suggesting an essential role for calcium in T2SS function.

To gain insight into the native pseudopilus structure and conformational dynamics during protein secretion, we solved the structure of the periplasmic PulG domain (PulGp) using NMR. We combined these data with a cryoEM map of purified PulG pili to generate T2SS pseudopilus atomic model. Furthermore, we characterized the role of calcium in PulG folding, stability and pseudopilus assembly *in vivo* and *in vitro*. Our structural and functional data suggests a role of calcium in pseudopilus folding, assembly and length control, with general implications for T2S mechanism.

Results

Calcium is required for PulG monomer and polymer stability

The calcium-binding site identified in the periplasmic domain of major pseudopilins from *Vibrio* and *E. coli* is highly conserved in its homologues, including PulG[10]. To test the effect of calcium depletion on PulG pilus assembly, an *E. coli* K-12 strain expressing all the *pul* genes encoding the *K. oxytoca* T2SS was grown in the presence of increasing concentrations of EGTA (Fig. 1b, WT). PulG cellular levels were dramatically reduced at EGTA concentrations of 1 mM or higher and pseudopilus assembly was abolished (Fig. 1b). As the *pulM* gene is located downstream of *pulG* in the same operon and encodes a T2SS component with the same topology as PulG (Fig. 1a), PulM levels were used as a control for *pul* gene expression. As expected, PulM was unaffected by the addition of EGTA. In the presence of 2 mM EGTA, PulG detection was rescued upon addition of Ca^{2+}, but not of Mg^{2+} or K^{+} (Fig. 1c). The PulG-FLAG variant was as sensitive to EGTA as $PulG^{WT}$, excluding the possibility that the lack of PulG detection was due to disruption of crucial epitopes recognized by anti-PulG antibodies (Fig. 1d). Addition of Ca^{2+} to the media restored piliation (Supplementary Fig. 1). Together, these data indicate that maintaining *in vivo* cellular levels of PulG depends on the presence of calcium and suggest that calcium depletion leads to PulG degradation.

Calcium depletion also affected the stability of PulG pseudopilus fibres *in vitro* (Fig. 1e). Upon incubation of purified pseudopili in buffer or buffer supplemented with Ca^{2+} for 1.5 or 18 hours, intact fibres were recovered in the pellet fraction following ultracentrifugation. In contrast, PulG was found in the supernatant fraction of pseudopili incubated in the presence of EGTA, indicating pseudopilus disassembly. Partial disassembly was observed for pili incubated for 18 hours in buffer, suggesting an exchange and gradual release of calcium. The disassembly was more dramatic after a long incubation with EGTA, whereas pseudopili

remained intact in buffer supplemented with Ca^{2+}. Together these data demonstrate that calcium is required for PulG stability *in vivo* and for the pseudopilus stability *in vitro*.

Essential role of calcium in PulG folding and stability

To understand the effect of calcium on PulG stability, solution NMR was used to analyse the structural features of the protein with and without calcium. For this study, we used the soluble periplasmic domain of PulG (residues 25-134), designated PulGp. The NMR spectral signature (^{15}N-^{1}H HSQC) of PulGp purified from the periplasm was unchanged after the addition of 1 mM calcium (Fig. 2a). In contrast, significant spectral changes were observed in the presence of 20 mM EGTA (PulGp-EGTA) (Fig. 2a). Addition of 1 mM calcium to the PulGp-EGTA sample, after EGTA was removed, restored the initial PulGp spectrum (Supplementary Fig. 2). These observations indicate that PulGp purified from the periplasm is calcium-bound and that this native folding is modified following calcium chelation by EGTA.

Further analyses comparing the ^{15}N-^{1}H HSQC spectrum of native PulGp with that of PulGp-EGTA highlight the structural role of calcium. The ^{15}N-^{1}H HSQC spectrum of native PulGp displayed good signal dispersion, typical of a well-structured protein. The number of peaks corresponded to those expected based on the protein sequence, indicating that only one conformer exists in the native condition. After calcium chelation by EGTA, the PulGp spectrum showed reduced signal dispersion and an increased number of peaks. The additional peaks appeared mainly between 7.7 and 8.7 ppm (Fig. 2a), indicating the presence of disordered regions in slow exchange on the chemical shift timescale between different conformations. To further characterize PulGp behaviour in the calcium-free state, its backbone resonances were assigned and used to estimate their secondary structure contents. Two conformers were identified (Fig. 2a). The first one with its backbone resonances almost entirely assigned (at 94%) displayed a slight decrease of secondary structure content in favour

of random coil (Supplementary Fig. 3a). The second conformer (assigned at 32%) is mostly disordered (Supplementary Fig. 3b). The propensity of PulGp to become partially unfolded or disordered in the absence of calcium shows the importance of this metal in protein folding and structural stability. In support of this conclusion, PulGp was thermostatically more stable in the presence of calcium, since its Tm increased by 17.2 °C, from 34°C in the calcium-free- to 51.8°C in the calcium-bound state (Supplementary Fig. 3c).

PulG calcium-binding site

To identify PulG residues affected by calcium, we analysed the chemical shift perturbation (CSP) of its amide resonances between the calcium-bound and -free states. C-terminal residues S113, L114, G115, D117, V119, D124, D125, I126 and G127 displayed the largest CSP (> 0.2 ppm, Fig. 2b), indicating that their chemical environment was modified either by their interaction with calcium or by conformational changes that were induced by the presence of calcium. Residues E121 and S122 in this region were also significantly perturbed, although their signals could not be unambiguously assigned in the calcium-free state.

To determine the effect of calcium binding *in vivo*, several PulG residues with high (113, 114, 117, 119, 124, 125), intermediate (131, 132), low (128, 129, 130, 133, 134) and undetermined (122) CSP values were individually substituted by an alanine. We analysed bacterial and pili fractions of strains containing PulG or PulG variants grown under pilus-inducing conditions (Fig. 2c). PulG levels were significantly affected by alanine substitutions of residues 113, 117, 122, 124, 125, 129 indicating their requirement for PulG stability *in vivo* and suggesting either direct involvement in calcium coordination or in intra-molecular contacts essential for PulG folding and stability.

Solution structure of PulGp in the calcium-bound state

Given the important role of calcium for native PulG folding in the periplasm, we solved the structure of PulGp in its calcium bound state. For this structure calculation, 2239 distance restraints, 44 hydrogen bonds and 156 dihedral angles were used. The details of restraints and structural characteristics of the family of 15 conformers representing the solution structure of PulGp are summarized in Supplementary Table 1. The structures display good convergence with a mean pairwise root mean square deviation (RMSD) of 0.5 and 1 Å for the backbone and the heavy atoms of ordered regions, respectively (Fig. 3a).

PulGp is a monomer in solution as indicated by its overall correlation time (7.8 ns). Its structure includes an N-terminal α-helix (α1, residues 29-54), a long αβ-loop (55-98) including a second α-helix (α2, residues 60-68), two short antiparallel β-strands (β1: 99-101 and β2: 110-112) and a short C-terminal helix (α3: 128 to 131) (Fig. 3b). Near the C-terminus, a long β2-α3 loop, well defined and convergent in the ensemble of conformers (Fig. 3a), harbours the calcium-binding site (Fig. 3c). It contains residues that exhibited the highest CSP values (Fig. 2b). In addition, other residues sensed the effect of calcium binding, as indicated by low but significant CSP values (Fig. 2b, 3c). They are located in the N-terminal α-helix (K30, D32, R33, Q34, V37), the C-terminal part of the αβ-loop and its junction with the β1 strand (D92, W94, S96, D97, Y98, Q99) and near the C-terminus (I131 and G132) (Fig. 3c). Although residue W129 is located outside the calcium-binding loop (Fig. 3c), its substitution by Ala abolished PulG detection (Fig. 2c). The proximity of W129 to H106 in the PulG structure (Supplementary Fig. 4a) suggested that stacking interactions between their aromatic rings flanking the β2-α3 loop stabilize the C-terminal region. Introducing Cys substitutions in both residues led to intra-molecular disulphide bond formation in variant $PulG^{H106C,W129C}$ allowing for pseudopilus assembly *in vivo* (Supplementary Fig. 4b).

Structure of the PulG pseudopilus

Recent advances in cryo-EM have provided an unprecedented insight into bacterial filaments[11]. We used cryo-EM to analyse purified pseudopili (Fig. 4a) formed by native PulG ($PulG^{WT}$) and by the $PulG^{H106C,W129C}$ variant ($PulG^{CC}$) containing an intra-molecular disulphide bond flanking the C-terminal Ca^{2+}-binding loop (Supplementary Fig. 4). The analysis of $PulG^{WT}$ and $PulG^{CC}$ fibres using the Iterative Helical Real Space Reconstruction (IHRSR) method[12] led to reconstructions that converged to highly similar helical parameters: a rise of 10.2 Å for both variants and twist angles of 83.5° and 83.2° for $PulG^{WT}$ and $PulG^{CC}$, respectively. The high degree of flexibility of $PulG^{WT}$ filaments, observed previously by negative staining EM[13], limits the resolution of the cryo-EM reconstruction. Although PulGp domain density is well defined in the cryo-EM map of $PulG^{WT}$ pili, with an estimated resolution of ~7 Å, the rod-shaped density of the N-terminal α-helix fades from residue G26 towards the N-terminus (Supplementary Fig. 5b), precluding the construction of an atomic model of this region. However, the cryo-EM map obtained for $PulG^{CC}$ has a higher resolution (~5 Å overall) (Fig. 4b-d) and the density for PulGp is extremely well-defined. The thinner density of the N-terminal α-helix at the junction with the PulGp could be connected to the region with characteristic helical-shaped density corresponding to the N-terminal PulG α helix (Fig. 4e) and allowed for unambiguous identification of individual PulG subunits.

The $PulG^{CC}$ pilus atomic model was built by refining, in the cryo-EM density map, the PulGp NMR structure connected to a model of the trans-membrane segment (TMS) by an extended (non-helical) linker (Fig. 4f). During refinement, the structure of PulGp was preserved, with a backbone RMSD of 2.1 Å between initial and final models for residues 27 to 130. The region surrounding the conserved P22 (from L19 to G26) has no regular secondary structure and residues 1-21 of the helical TMS fit nicely in the N-terminal density (Fig 4e). In the final atomic model, the $PulG^{CC}$ pilus has a diameter of around 70 Å (Fig. 4d) and contacts between PulG subunits P and P+1, P+3 and P+4 are observed along the right-

handed 1-start helix (Fig. 5a). The globular domains form an outer ring whereas the TMSs are packed at the pilus core and the calcium-binding loop is on the pilus surface (Fig. 5b). Residues conserved in the major pseudopilin family are located in the core of the pilus while surface-exposed residues are mostly non-conserved (Supplementary Fig. 6a). The inner side of the PulG subunit facing the core of the pilus shows a stretch of conserved, mostly hydrophobic residues (Supplementary Fig. 6b).

Both the $PulG^{WT}$ and $PulG^{CC}$ pili displayed similar subunit organization, with PulG subunits forming contacts *via* the PulGp domains, the hydrophobic domains, as well as between PulGp and hydrophobic domains (Fig. 5 and Supplementary Fig. 7). The cryo-EM reconstruction of $PulG^{WT}$ and $PulG^{CC}$ supports the proximity of residues 10_{P+1} and 16_P, consistent with efficient cross-linking of PulG variants with Cys at these positions (Cβ-Cβ distance of 6.9 Å), but not with Cys substitutions at positions 7 and 13 (distance of 11.3 Å) used as a control[14] (Fig. 5d,e).

The atomic model of the $PulG^{CC}$ pilus fits well into the ~7 Å cryo-EM map of $PulG^{WT}$ (cross-correlation coefficient of 0.76 after rigid docking) where the unstructured L19-G26 region sits in the central thin density and the helical N-terminal portion of the TMS is positioned in the rod-like density at the core of the map (Supplementary Fig. 5b). Inter-subunit contacts between conserved residues of TMSs and PulGp predicted by co-evolutionary analysis are also observed in the structure, further supporting the $PulG^{CC}$ atomic model (Supplementary Fig. 6e). Therefore, with the exception of the disulphide bond, the atomic model of $PulG^{CC}$ is a good model for the native PulG pilus structure.

Discussion

We report the structures of the PulG monomer and homo-polymer that constitute the core of the pseudopilus, an essential T2SS sub-complex. We demonstrate the key role of calcium in pseudopilus biogenesis, folding and stability, explaining the previously described role of calcium in protein secretion[10].

The structure of the periplasmic PulG monomer was identical to that of the calcium-bound state formed *in vitro*, showing that calcium induces native PulG folding and is required for its stability. Calcium depletion destabilized PulG *in vitro*, yielding two different non-native conformations, which coexist and exchange with a rate slower than a millisecond. Remarkably, the addition of calcium to these calcium-free conformations restored the native fold. Calcium-dependent PulG folding may explain differences between the NMR and X-ray structures solved respectively with and without calcium. Under NMR experimental conditions PulGp is a monomer, whereas it is observed as a domain swapped PulGp dimer in the crystal [9]. The major differences between the PulGp NMR and crystal structure are found along the C-terminus including the calcium-binding region (RMSD of 13 Å for residues 124-133, versus 3 Å for the rest of the protein). In the NMR structure, the PulGp C-terminus is in a helical conformation, whereas in the X-ray structure two β strands are present (Fig. 3 and Supplementary Fig. 8). Strikingly, EGTA treatment resulted in the formation of a shorter loop followed by a β3 strand in the more folded PulGp conformer (Supplementary Fig. 3a) reminiscent of the X-ray structure.

When comparing available structures of major pseudopilin homologues the conformation of the C-terminal part, either as α-helix or β-strand, correlates with the presence of calcium[10,15]. The orientation of the β1-β2 loop in these structures is similarly influenced by the presence of calcium (Supplementary Fig. 8). Interestingly, the NMR structure of native PulGp is more similar to the X-ray structures of EHEC and *V. cholerae* pseudopilins obtained with calcium (DALI server Z score of 14.4 and 13.4 over 107 aligned residues) than to its

own X-ray structure (Z score of 11.8). While the structural effect of calcium is reversible, calcium depletion and Ala substitutions of calcium-coordinating residues *in vivo* led to PulG degradation and abolished T2SS function. These data support an important regulatory role of calcium levels, which are known to influence expression or activity of many bacterial virulence-related secretion systems[16-18] and adherence factors[19,20], during adaptation to specific niches or lifestyles[21].

The structure of the calcium-bound form of PulGp fits well into the cryoEM map of the PulG pseudopilus, and all residues can be assigned a density, except for the four C-terminal residues, suggesting high flexibility. The helical symmetry of fibres formed by both $PulG^{WT}$ and $PulG^{CC}$ is very close to previously reported values from STEM[9] and negative stain EM[13] (Fig. 4b,c and Supplementary Fig. 9f). Compared to our previous models[14], we observe a major structural change involving parts of the N-terminal domain (Supplementary Fig. 9a-c). The cryoEM structure shows that the central region of the pilus stem (L19-G26) is non-helical and shifted downwards by ~7 Å along the pilus axis with respect to PulGp. Several algorithms predict low helical propensity for this region (Supplementary Fig. 6d). A similar feature of the α-helical stem was previously observed between residues 15 to 23 in the major subunit PilE of meningococcal T4P[22], despite having different subunit packing, and in an EHEC pseudopilin crystal structure[10] (Supplementary Fig. 9d,e). The X-ray structure of the *Neisseria gonorrhoeae* pilin[23], which was the basis of PulG model used for our previous pseudopilus model[14] shows a long continuous helix, which is also present in the NMR structure of the *Geobacter* pilin in solution[24]. These structures display the all-helical conformation that is likely present in the membrane prior to assembly, as also suggested by PulG molecular dynamics simulations[25]. Direct observation of this non-helical, extended conformation in the pseudopilus suggests a structural modification, potentially induced during

the membrane extraction step of fibre assembly[25], whose mechanism and function remain to be explored.

The pseudopilus cryoEM reconstruction provides the comprehensive description of potential inter-protomer contacts. This structure is consistent with highly conserved pseudopilus salt-bridges involving negatively charged residues (44 and 48) of protomer P and positively charged residues (87 and 88) of protomer P+1, extensively validated by mutagenesis[14] (Fig. 5c and Supplementary Fig.6e) and essential for PulG dimer formation in the membrane[13], pseudopilus assembly and protein secretion[14]. Other long-range contacts specifically involved in pseudopilus stability are consistent with the cryoEM structure, including $K30_{P+3}$ and $D53_{P}$ [13].

The high flexibility of T4P-like fibres, crucial for assembly and function, limits their resolution by cryoEM. Here the $PulG^{CC}$ variant allowed for increased resolution over the wild type. Although the overall fold of $PulG^{CC}$ subunit is conserved, the dynamics of its C-terminal region constrained by the disulphide bond seems to have a global destabilizing effect since $PulG^{CC}$ fibres are less stable and, compared to the native fibres, disassemble more readily due to calcium release (Supplementary Fig. 10).

By analogy to the closely related T4P, which extend and retract through the action of two antagonistic ATPases, it has been proposed that the pseudopilus promotes protein secretion in a piston-like fashion[26,27]. However, T2SSs only have one assembly ATPase, raising a question of the pseudopilus disassembly mechanism. In the alternative Archimedes' screw model, pseudopilus assembly at the base is coupled to its disassembly and degradation at the fibre tip[13]. T2SS overproduction and plate culture promote pseudopilus extension beyond the bacterial surface[5,28,29]. However, under liquid culture conditions that promote exoprotein secretion, pseudopili are not detected on the cell surface suggesting a length control mechanism. Fibre disassembly in the absence of calcium shown here provides a

mechanistic basis for pseudopilus length control. While continuous addition of pseudopilin subunits to the base of the fibre in the membrane drives protein secretion[13], pseudopilins at the tip would be the first to encounter the extracellular environment, where calcium levels could be locally lower than in the periplasm[30]. These conditions combined with dynamic interactions with T2SS components or substrates would favour subunit dissociation and proteolysis [31]. The pseudopilus structure determined in this work, combined with NMR and other tools to study interactions with T2SS components and substrates provides an ideal framework to elucidate the protein secretion mechanism.

Methods

Bacterial strains, plasmids and molecular biology techniques

E. coli strains and plasmids used in this study are listed in Supplementary Table 2. Bacteria were grown on LB media at 30°C or 37°C on LB medium supplemented, as required, with 100 $\mu g.ml^{-1}$ ampicillin (Ap) or 25 $\mu g.ml^{-1}$ chloramphenicol (Cm). DNA manipulations and transformation were performed as described[32]. Modified Quick-Change method and primers listed in Supplementary Table 2 were used for site-directed mutagenesis. All constructs were verified by DNA sequencing (Eurofins and GATC).

Pilus assembly and stability assays

Pseudopilus assembly assays were performed as described previously. Briefly, *E. coli* strain PAP7460 containing indicated plasmids were grown at 30°C for 48 hr on LB agar containing 0.2% D-maltose, Ap and Cm [14]. Proteins were analysed by denaturing polyacrylamide gel electrophoresis (PAGE) on 10% Tris-Tricine gels[33], transferred onto nitrocellulose membranes (ECL, Amersham) and processed for immunoblot. Custom-made polyclonal anti-

PulG (Genscript) and anti-PulM antisera were used as described[34]. Monoclonal anti-FLAG M2 antibodies (Sigma F-3165) were used at a working concentration of 0.8 $\mu g.ml^{-1}$. Secondary goat anti-rabbit or anti-mouse secondary antibodies coupled to HRP (GE) were diluted to 1:20000. Blots were revealed by ECL2 (Thermo) and fluorescence signal was recorded on Typhoon FLA7000 phosphorimager (GE). Images were processed using Adobe Photoshop.

Pseudopili were purified from *E. coli* strains PAP7460 containing appropriate plasmids (Supplementary Table 2) as described[9]. Pili were stored in HS buffer (50 mM HEPES pH 7.2, 50 mM NaCl) at 4°C and used for cryoEM or stability assays. For pilus stability experiments, HS buffer was supplemented with 5 mM $CaCl_2$ or 5 mM EGTA and incubated for 1.5-18 hrs. The samples were subjected to ultracentrifugation for 30 min at 53 krpm in TLA-55 Beckmann rotor. Supernatant and pellet fractions were boiled in protein sample buffer for 5 min, and analysed by PAGE on 10% polyacrylamide Tris-Tricine gels[33]. Proteins were visualized upon staining with Coomassie blue R.

Expression and purification of isotope-labelled PulGp domain

The PulG hydrophobic segment (residues 1-24) in pMS153, containing a cleavable PelB signal peptide followed by a hexa-His tag fused to mature PulG was replaced by a TEV cleavage site to generate plasmid pMS155, allowing us to produce the soluble PulG domain (residues 25 through 134, hereafter called PulGp) in the periplasm. A C-terminal His_6-tagged version of PulGp described previously[9] was used for structure determination. Protein expression, labelling and purification were performed as previously described[35]. The concentration of purified PulGp was determined from its absorbance at 280 nm and a calculated extinction coefficient of 18 450 M^{-1} cm^{-1}.

NMR spectroscopy

The NMR samples were maintained in 50 mM HEPES buffer, pH 7, 50 mM NaCl, 10% D_2O, supplemented with 1 mM $CaCl_2$ or 20 mM EGTA as required. All NMR experiments used for structure calculation were recorded in the presence of 1 mM $CaCl_2$, to ensure the calcium bound state of the protein. PulGp concentrations were between 0.5 and 0.6 mM. NMR experiments were acquired at 298 K on a Varian spectrometer operating at 600 MHz (^{1}H frequency) and equipped with a triple resonance cryogenically cooled ^{1}H {^{13}C/^{15}N} PFG probe. 2, 2-dimethyl-2-silapentane-5-sulfonate (DSS) signal was taken as 0 ppm for referencing ^{1}H chemical shifts and ^{15}N and ^{13}C chemical shifts were indirectly referenced to DSS[36]. The pulse sequences were employed as implemented in the Agilent BioPack *(www.chem.agilent.com).* NMR Pipe[37] and CcpNmr Analysis[38] were used for NMR data processing and analysis, respectively. 3D ^{13}C and ^{15}N NOESY-HSQC experiments with mixing times of 120 ms were recorded on a Bruker AVANCE III 950 MHz equipped with a TCI probe. In this case, the data was acquired and processed with TOPSPIN 3.1 (*Bruker, Germany*). Resonance assignments were obtained from the analysis of standard NMR experiments as previously described[35].

PulGp calcium binding monitored by NMR

^{1}H-^{15}N HSQC experiments (1024 x 128 data points) were acquired on 0.5 mM PulGp in 50 mM HEPES buffer, pH 7, 50 mM NaCl, supplemented by 1 mM $CaCl_2$ or 20 mM EGTA. Chemical shift perturbations (CSP) of PulGp backbone amide cross-peaks were quantified by using the equation $CSP = [\Delta\delta H^2 + (\Delta\delta N*0.159)^2]^{1/2}$, where $\Delta\delta$ H and $\Delta\delta$ N are the observed ^{1}H and ^{15}N chemical shift changes between the two experimental conditions. For the calcium-free state (in the presence of EGTA), only the conformer for which 94% of backbone resonances were assigned was considered. The secondary structure content of PulGp

conformers in the calcium-free and bound states were estimated based on the backbone chemical shifts with the TALOS-N software[39].

NMR structure calculation

We determined the structure of PulGp in the calcium bound state by performing several cycles of calculation with ARIA 2.3 software[40] coupled to CNS 1.2 software[41], making use of the standard torsion angle/Cartesian simulating annealing protocol. Each cycle consisted of automatic NOESY assignment and structure calculations with 9 iterations with default parameters. In the last iteration 200 structures were calculated and further refined in an explicit water box[42]. The 15 lowest energy structures exhibiting no NOE restraint violations > 0.5 Å and no dihedral angle violations > 5° were selected as the final ensemble.

Distance restraints were derived from 3D ^{13}C and ^{15}N NOESY-HSQC experiments, by making use of the almost complete PulGp resonances assignment previously reported[35]. Chemical shift tolerances were set to 0.045 for protons and 0.4 ppm for the heteroatoms. Phi and psi dihedral angles were predicted with TALOS-N[39] and predictions classified as "strong" were incorporated as dihedral angle restraints. Hydrogen bonds predicted from H/D exchange experiments and supported by characteristic secondary structure NOE patterns were included as restraints in the last cycles of calculations. Hydrogen bonds typical of antiparallel β-sheet were incorporated for pairing residues 99-101 to residues 110-112 as well as for residue 33 to 54 of α-helix. Spin diffusion correction was applied as implemented in ARIA by using the τc of PulGp (7.8 ns) obtained from ^{15}N spin-relaxation data.

The calcium atom was coordinated by the side chain oxygen of residues D117, S122 and D125, and backbone carbonyl oxygen of residues L114 and V119. The coordination scheme was set up as described for calcium-bound X-ray structures of homologous major

pseudopilins[10] and supported by the PulGp-calcium/EGTA CSP results. The geometry of the calcium coordination was maintained by imposing fixed distances between the calcium ion and the above-mentioned oxygen atoms. Proline residues 75 and 103 were defined in *cis* configuration based on their backbone chemical shifts and predictions using Promega software[43]. The structure ensemble was visualized and inspected with PyMOL[44] and the quality was evaluated with PROCHECK-NMR[45] and the PSVS server[46]. The structure atomic coordinates and restraints used in the calculation were deposited in the Protein Data Bank (PDB id: 5O2Y). We estimated the global rotation correlation time (τc) of the protein after the measurement of ^{15}N relaxation parameters assuming an isotropic tumbling model and using the program Tensor2[47] as described previously[48].

Circular dichroism (CD)

Far-UV CD spectra were recorded on an Aviv 215 spectropolarimeter equipped by a Peltier thermostated cell holder *(Aviv Biomedical)* and in 1 mm cell. Protein sample were at 50 µM in 50 mM Hepes, pH 7, 50 mM NaCl, supplemented by 1 mM $CaCl_2$ or 1 mM EGTA. Thermal denaturation of PulG was performed by heating the samples from 15 to 98°C, with an increment of 1°C and an average time of 2 s per step. The PulGp melting temperature (Tm) in each buffer condition was determined from the denaturation curves obtained by measuring ellipticity at 222 nm.

CryoEM data collection and image processing

The PulG sample (3µL, double mutant H106C-W129C) was applied to glow-discharged lacey carbon grids (TED PELLA, Inc., 300 mesh). Then the grids were plunged frozen using a Vitrobot Mark IV (FEI, Inc.), and subsequently imaged in a Titan Krios at 300keV with a Falcon II direct electron detector (pixel size 1.05 Å /pixel). A total of 1,819 images, each of

which was from a total exposure of 2 seconds dose-fractionated into seven chunks, were collected and motion corrected using MotionCorr[49]. Program CTFFIND3[50] was used for determining the defocus and astigmatism. Images with poor CTF estimation as well as defocus > 3μm were discarded. The SPIDER software package[51] was used for most other operations. The CTF was corrected by multiplying the images from the first two chunks (containing a dose of ~ 20 electrons/ $Å^2$) with the theoretical CTF, which is a Wiener filter in the limit of a very poor signal-to-noise ratio (SNR). This both corrects the phases, which need to be flipped, and improves the SNR. The e2helixboxer routine within EMAN2[52] was used for boxing the filaments from the images. A total of 85,619 overlapping segments (384 px long), with a shift of 14 px between adjacent segments (~96% overlap), were used for the IHRSR[12] reconstruction. The resolution of the reconstruction was determined by the FSC between two independent half maps, generated from two non-overlapping data sets, which was ~5 Å at FSC=0.143.

Model building and refinement

The PulGp NMR structure was docked in the cryo-EM map of $PulG^{H106CW129C}$ by rigid-body docking with the program Situs[53]. Next, we generated a homology model of PulG N-terminal α-helical residues (T2-V20) with the software Modeller [54] based on the structure of the *Pseudomonas* PAK pilin (PDB 1OQW) as template. This model of the PulG N-terminal helix was rigidly docked in the remaining density of the cryo-EM map (not occupied by PulGp) with Situs[53] (residues 25-26 were not included since they are not ordered in the NMR ensemble). A full-length model of PulG was then constructed with Modeller[54] by connecting the docked PulGp and N-terminal helix with an extended linker (V21-G26) and adding F1. Side-chains of H106 and W129 were replaced by a Cysteine side-chain and a methyl group was added to the N-terminal Phe (N-methylphenylalanine). Density for the four C-terminal

residues is absent in the cryo-EM map and these residues were excluded. Next, the full-length model of PulG^{CC} was refined in the density map with CNS[55]. Energy minimization followed by torsion-angle MD simulated-annealing in the presence of stereo-chemical restraints was performed with the real-space objective function calculated by RSRef[56] in CNS. Helical symmetry of the pilus was imposed with strict NCS constraints using the symmetry parameters of the experimental cryoEM map. Refinement with RSRef was repeated 1000 times with different random seeds and the lowest energy model was selected for further refinement. Next, several cycles of geometry optimization and full-atom real-space refinement with PHENIX [57] followed by manual inspection in Coot[58] were performed to improve the fit to the experimental cryo-EM map and remove severe steric clashes and outliers. The final model of PulG pilus was validated with Molprobity[59] and refinement statistics are given in Supplementary Table 3. Figures were generated with UCSF Chimera[60] and PyMOL[44].

Analysis of residue conservation, co-evolutionary analysis and helical propensity

Residue conservation of PulG sequence was obtained with the Consurf server [61] (300 homologous sequences asked with between 35 and 95% identity). Co-evolutionary contact predictions for PulG were obtained with the Gremlin tool[62]. The ratio between the number of sequences used by Gremlin and the length of the query was 14.9. Helical propensity of PulG residues F1-R56 was computed with the PSIPRED[63] and Jpred4[64] servers; the alpha-helical scale of Chou & Fasman[65] was used to create the profile shown in Supplementary Fig. 6d.

Data availability

The data that support the findings of this study are available from the corresponding authors upon request. The PulGp structure is available in the Protein Data Bank (accession code

5O2Y). The PulG pseudopilus cryo-EM map and model have been deposited to EMDB and PDB, with codes EMD-8812 and 5WDA respectively.

References

1. Berry, J.L. & Pelicic, V. Exceptionally widespread nanomachines composed of type IV pilins: the prokaryotic Swiss Army knives. *FEMS Microbiol. Rev.* **39**, 134-54 (2015).
2. Jarrell, K.F. & Albers, S.V. The archaellum: an old motility structure with a new name. *Trends Microbiol.* **20**, 307-12 (2012).
3. Thomassin, J.L., Santos Moreno, J., Guilvout, I., Tran Van Nhieu, G. & Francetic, O. The trans-envelope architecture and function of the type 2 secretion system: new insights raising new questions. *Mol. Microbiol.* **105**, 211-226 (2017).
4. Cianciotto, N.P. & White, R.C. Expanding role of type II secretion in bacterial pathogenesis and beyond. *Infect. Immun.* **85,** pii: e00014-17 (2017).
5. Sauvonnet, N., Vignon, G., Pugsley, A.P. & Gounon, P. Pilus formation and protein secretion by the same machinery in *Escherichia coli*. *EMBO J.* **19**, 2221-8 (2000).
6. Korotkov, K.V. & Hol, W.G. Structure of the GspK-GspI-GspJ complex from the enterotoxigenic *Escherichia coli* type 2 secretion system. *Nat. Struct. Mol. Biol.* **15**, 462-8 (2008).
7. Cisneros, D.A., Bond, P.J., Pugsley, A.P., Campos, M. & Francetic, O. Minor pseudopilin self-assembly primes type II secretion pseudopilus elongation. *EMBO J.* **31**, 1041-53 (2012).
8. Korotkov, K.V., Sandkvist, M. & Hol, W.G. The type II secretion system: biogenesis, molecular architecture and mechanism. *Nat. Rev. Microbiol.* **10**, 336-51 (2012).
9. Kohler, R. *et al*. Structure and assembly of the pseudopilin PulG. *Mol. Microbiol.* **54**, 647-64 (2004).
10. Korotkov, K.V. *et al*. Calcium is essential for the major pseudopilin in the type 2 secretion system. *J. Biol. Chem.* **284**, 25466-70 (2009).
11. Egelman, E.H. Cryo-EM of bacterial pili and archaeal flagellar filaments. *Curr. Op. Struct. Biol.* **46**, 31-37 (2017).
12. Egelman, E.H. A robust algorithm for the reconstruction of helical filaments using single-particle methods. *Ultramicroscopy* **85**, 225-34 (2000).
13. Nivaskumar, M. *et al.* Distinct docking and stabilization steps of the pseudopilus conformational transition path suggest rotational assembly of type IV pilus-like fibers. *Structure* **22**, 685-96 (2014).
14. Campos, M., Nilges, M., Cisneros, D.A. & Francetic, O. Detailed structural and assembly model of the type II secretion pilus from sparse data. *Proc. Natl. Acad. Sci. USA* **107**, 13081-6 (2010).
15. Alphonse, S. *et al*. Structure of the *Pseudomonas aeruginosa* XcpT pseudopilin, a major component of the type II secretion system. *J. Struct. Biol.* **169**, 75-80 (2010).
16. Williams, A.W. & Straley, S.C. YopD of *Yersinia pestis* plays a role in negative regulation of the low-calcium response in addition to its role in translocation of Yops. *J. Bacteriol.* **180**, 350-8 (1998).

17. Lu, D. *et al.* Structural insights into the T6SS effector protein Tse3 and the Tse3-Tsi3 complex from *Pseudomonas aeruginosa* reveal a calcium-dependent membrane-binding mechanism. *Mol. Microbiol.* **92**, 1092-112 (2014).
18. O'Brien, D.P. *et al.* Structural models of intrinsically disordered and calcium-bound folded states of a protein adapted for secretion. *Sci Rep* **5**, 14223 (2015).
19. Bilecen, K. & Yildiz, F.H. Identification of a calcium-controlled negative regulatory system affecting *Vibrio cholerae* biofilm formation. *Environ. Microbiol.* **11**, 2015-29 (2009).
20. Orans, J. *et al*. Crystal structure analysis reveals *Pseudomonas* PilY1 as an essential calcium-dependent regulator of bacterial surface motility. *Proc. Natl. Acad. Sci. USA* **107**, 1065-70 (2010).
21. Broder, U.N., Jaeger, T. & Jenal, U. LadS is a calcium-responsive kinase that induces acute-to-chronic virulence switch in *Pseudomonas aeruginosa*. *Nat. Microbiol.* **2**, 16184 (2016).
22. Kolappan, S. *et al.* Structure of the *Neisseria meningitidis* Type IV pilus. *Nat. Commun.* **7**, 13015 (2016).
23. Craig, L. *et al.* Type IV pilus structure by cryo-electron microscopy and crystallography: implications for pilus assembly and functions. *Molecular Cell* **23**, 651-62 (2006).
24. Reardon, P.N. & Mueller, K.T. Structure of the type IVa major pilin from the electrically conductive bacterial nanowires of *Geobacter sulfurreducens*. *J. Biol. Chem.* **288**, 29260-6 (2013).
25. Santos-Moreno, J. *et al.* Polar N-terminal residues conserved in Type 2 secretion pseudopilins determine subunit targeting and membrane extraction steps during fibre assembly. *J. Mol. Biol.* **429**, 1746-1765 (2017).
26. Shevchik, V.E., Robert-Baudouy, J. & Condemine, G. Specific interaction between OutD, an *Erwinia chrysanthemi* outer membrane protein of the general secretory pathway, and secreted proteins. *EMBO J.* **16**, 3007-16 (1997).
27. Sandkvist, M. Biology of type II secretion. *Mol. Microbiol.* **40**, 271-83 (2001).
28. Durand, E. *et al.* Type II protein secretion in *Pseudomonas aeruginosa*: the pseudopilus is a multifibrillar and adhesive structure. *J Bacteriol.* **185**, 2749-58 (2003).
29. Vignon, G. *et al.* Type IV-like pili formed by the type II secreton: specificity, composition, bundling, polar localization, and surface presentation of peptides. *J. Bacteriol.* **185**, 3416-28 (2003).
30. Jones, H.E., Holland, I.B. & Campbell, A.K. Direct measurement of free $Ca^{(2+)}$ shows different regulation of $Ca^{(2+)}$ between the periplasm and the cytosol of *Escherichia coli*. *Cell Calcium* **32**, 183-92 (2002).
31. East, A. *et al.* Structural basis of pullulanase membrane binding and secretion revealed by X-ray crystallography, molecular dynamics and biochemical analysis. *Structure* **24**, 92-104 (2016).
32. Sambrook, J., Fritsch, E.F. & Maniatis, T. *Molecular cloning : a laboratory manual*, (Cold Spring Harbor Laboratory Press, Cold Spring Harbor, 1989).
33. Schagger, H. Tricine-SDS-PAGE. *Nat. Protoc.* **1**, 16-22 (2006).
34. Nivaskumar, M. *et al.* Pseudopilin residue E5 is essential for recruitment by the type 2 secretion system assembly platform. *Mol. Microbiol.* **101**, 924-41 (2016).
35. Lopez-Castilla, A. *et al.* ^{1}H, ^{15}N and ^{13}C resonance assignments and secondary structure of PulG, the major pseudopilin from *Klebsiella oxytoca* type 2 secretion system. *Biomol. NMR Assign.* doi: 10.1007/s12104-017-9738-7 (2017).

36. Wishart, D.S. *et al.* ^{1}H, ^{13}C and ^{15}N chemical shift referencing in biomolecular NMR. *J. Biomol. NMR* **6**, 135-40 (1995).
37. Delaglio, F. *et al.* NMRPipe: a multidimensional spectral processing system based on UNIX pipes. *J. Biomol. NMR* **6**, 277-93 (1995).
38. Vranken, W.F. *et al.* The CCPN data model for NMR spectroscopy: development of a software pipeline. *Proteins* **59**, 687-96 (2005).
39. Shen, Y. & Bax, A. Protein backbone and sidechain torsion angles predicted from NMR chemical shifts using artificial neural networks. *J. Biomol. NMR* **56**, 227-41 (2013).
40. Rieping, W. *et al.* ARIA2: automated NOE assignment and data integration in NMR structure calculation. *Bioinformatics* **23**, 381-2 (2007).
41. Brunger, A.T. *et al.* Crystallography & NMR system: A new software suite for macromolecular structure determination. *Acta Crystallogr. D Biol. Crystallogr.* **54**, 905-21 (1998).
42. Linge, J.P., Williams, M.A., Spronk, C.A., Bonvin, A.M. & Nilges, M. Refinement of protein structures in explicit solvent. *Proteins* **50**, 496-506 (2003).
43. Shen, Y. & Bax, A. Prediction of Xaa-Pro peptide bond conformation from sequence and chemical shifts. *J. Biomol. NMR* **46**, 199-204 (2010).
44. Schrödinger, L. The PyMOL Molecular Graphics System, Version 1.8. (2015).
45. Laskowski, R.A., Rullmannn, J.A., MacArthur, M.W., Kaptein, R. & Thornton, J.M. AQUA and PROCHECK-NMR: programs for checking the quality of protein structures solved by NMR. *J. Biomol. NMR* **8**, 477-86 (1996).
46. Bhattacharya, A., Tejero, R. & Montelione, G.T. Evaluating protein structures determined by structural genomics consortia. *Proteins* **66**, 778-95 (2007).
47. Dosset, P., Hus, J.C., Blackledge, M. & Marion, D. Efficient analysis of macromolecular rotational diffusion from heteronuclear relaxation data. *J. Biomol. NMR* **16**, 23-8 (2000).
48. Wolff, N. *et al.* Comparative analysis of structural and dynamic properties of the loaded and unloaded hemophore HasA: functional implications. *J. Mol. Biol.* **376**, 517-25 (2008).
49. Li, X. *et al.* Electron counting and beam-induced motion correction enable near-atomic-resolution single-particle cryo-EM. *Nat. Methods* **10**, 584-90 (2013).
50. Mindell, J.A. & Grigorieff, N. Accurate determination of local defocus and specimen tilt in electron microscopy. *J. Struct. Biol.* **142**, 334-347 (2003).
51. Frank, J. *et al.* SPIDER and WEB: Processing and visualization of images in 3D electron microscopy and related fields. *J. Struct. Biol.* **116**, 190-199 (1996).
52. Tang, G. *et al.* EMAN2: an extensible image processing suite for electron microscopy. *J. Struct. Biol.* **157**, 38-46 (2007).
53. Wriggers, W. Conventions and workflows for using Situs. *Acta Crystallogr. D Biol. Crystallogr.* **68**, 344-51 (2012).
54. Sali, A. & Blundell, T.L. Comparative protein modelling by satisfaction of spatial restraints. *J. Mol. Biol.* **234**, 779-815 (1993).
55. Brunger, A.T. Version 1.2 of the Crystallography and NMR system. *Nat. Protoc.* **2**, 2728-33 (2007).
56. Chapman, M.S., Trzynka, A. & Chapman, B.K. Atomic modeling of cryo-electron microscopy reconstructions--joint refinement of model and imaging parameters. *J. Struct. Biol.* **182**, 10-21 (2013).
57. Adams, P.D. *et al.* PHENIX: a comprehensive Python-based system for macromolecular structure solution. *Acta Crystallogr. D Biol. Crystallogr.* **66**, 213-21 (2010).

58. Emsley, P., Lohkamp, B., Scott, W.G. & Cowtan, K. Features and development of Coot. *Acta Crystallogr. D Biol. Crystallogr.* **66**, 486-501 (2010).
59. Davis, I.W. *et al.* MolProbity: all-atom contacts and structure validation for proteins and nucleic acids. *Nucleic Acids Res.* **35**, W375-83 (2007).
60. Pettersen, E.F. *et al.* UCSF Chimera - a visualization system for exploratory research and analysis. *J. Comput. Chem.* **25**, 1605-12 (2004).
61. Ashkenazy, H. *et al.* ConSurf 2016: an improved methodology to estimate and visualize evolutionary conservation in macromolecules. *Nucleic Acids Res.* **44**, W344-50 (2016).
62. Kamisetty, H., Ovchinnikov, S. & Baker, D. Assessing the utility of coevolution-based residue-residue contact predictions in a sequence- and structure-rich era. *Proc. Natl. Acad. Sci. USA* **110**, 15674-9 (2013).
63. Jones, D.T. Protein secondary structure prediction based on position-specific scoring matrices. *J. Mol. Biol.* **292**, 195-202 (1999).
64. Drozdetskiy, A., Cole, C., Procter, J. & Barton, G.J. JPred4: a protein secondary structure prediction server. *Nucleic Acids Res.* **43**, W389-94 (2015).
65. Chou, P.Y. & Fasman, G.D. Prediction of the secondary structure of proteins from their amino acid sequence. *Adv. Enzymol. Relat. Areas Mol. Biol.* **47**, 45–148 (1978).

Correspondence and requests for materials should be addressed to: Olivera Francetic (olivera.francetic@pasteur.fr) and Nadia Izadi-Pruneyre (nadia.izadi@pasteur.fr).

Acknowledgements

This work was funded by the Institut Pasteur, the Centre National de la Recherche Scientifique (CNRS), the French Agence Nationale de la Recherche (ANR-14-CE09-0004), the European Union FP7-IDEAS-ERC 294809 (to M. Nilges) and the NIH R35GM122510 (to E.H.E.). We thank Léa Khoury for help in sample preparation, the Plateforme de Biophysique Moléculaire of Institut Pasteur and Bruno Baron for assistance in CD experiments. We are grateful to Muriel Delepierre and Daniel Ladant for support and interest in this work. We acknowledge Nelly Morellet and financial support from the TGIR-RMN-THC Fr3050 CNRS.

Author contributions

644 Conceived and designed the experiments: ALC, JLT, BB, M. Nilges, EHE, NIP and OF.

645 Performed the experiments: ALC, JLT, BB, WZ, XY, M. Nivaskumar. Analysed the data and

646 wrote the manuscript: ALC, JLT, BB, WZ, M. Nilges, EHE, NIP and OF.

647

Figures

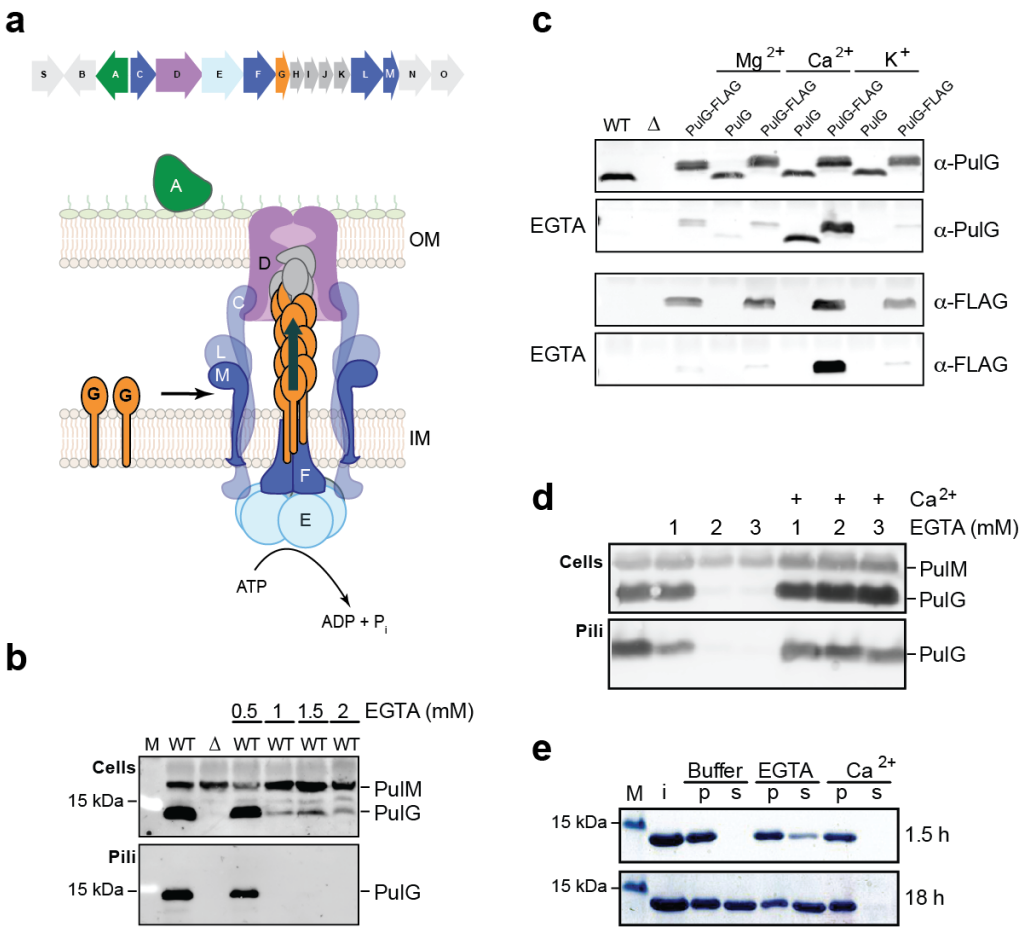
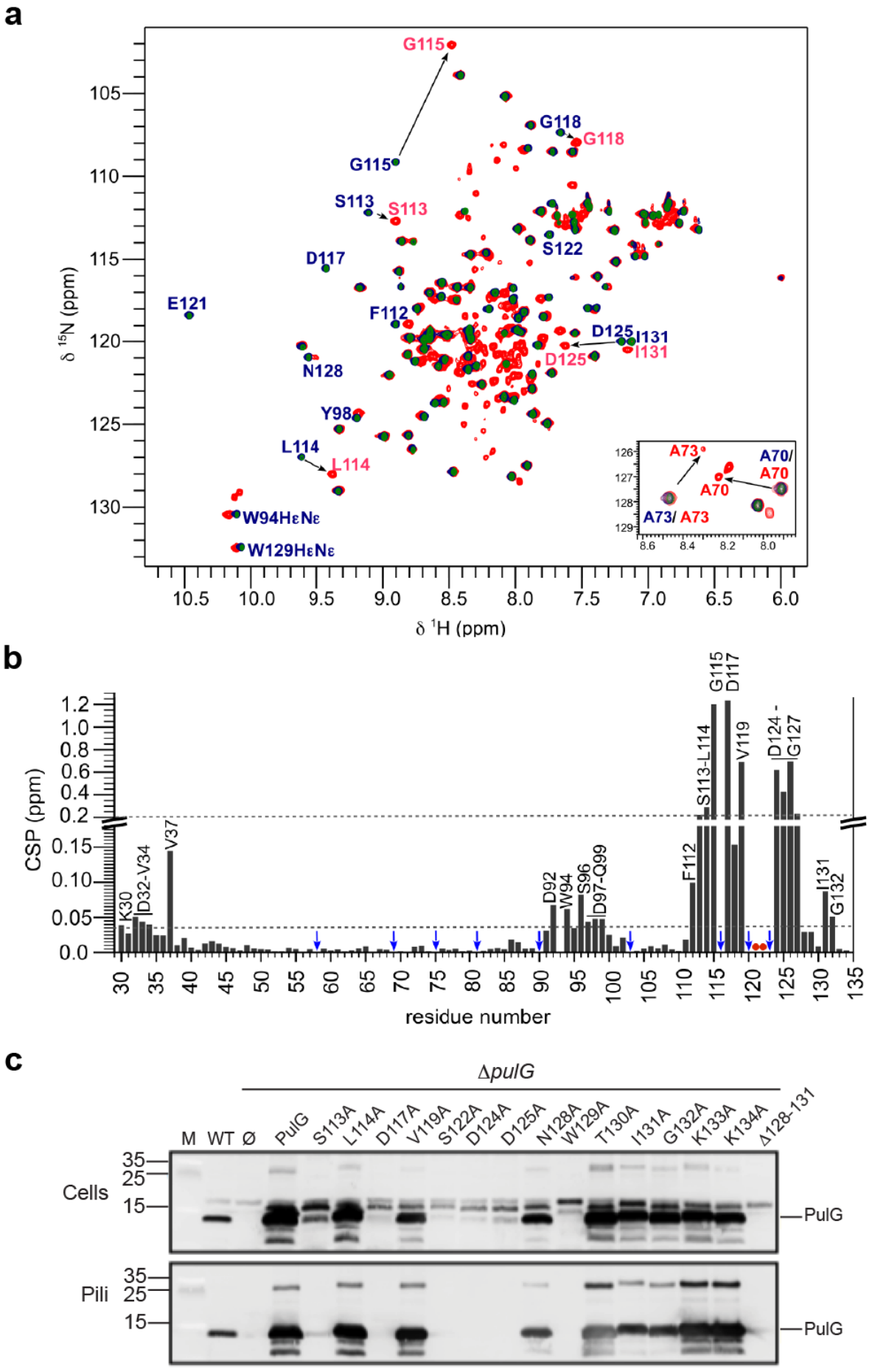


Figure 1. Calcium is required for PulG stability, pseudopilus assembly and stability. **a**, Top: cartoon of the gene organization in the *pul* cluster. Bottom: a schematic view of the assembled T2SS nanomachine, with individual components labelled with the corresponding single-letter and colour code. **b**, **c**, **d**, PAP7460 harbouring pCHAP8185 and pSU19 (WT), pCHAP8184 and pSU19 (Δ*pulG*; Δ), pCHAP8184 and pCHAP8658 (PulG), or pCHAP8184 and pCHAP5247 (PulG-FLAG) were grown under pilus-inducing conditions in media supplemented with EGTA and/or cations as indicated. Where appropriate, molecular weight markers (M) are indicated on the left in kDa. **b**, Effect of EGTA on T2SS function was monitored by probing cell extract and sheared pilus fractions with anti-PulG and anti-PulM antibodies. **c**, Effect of different cations on total PulG levels was monitored in bacterial cells using PulG (α-PulG) and FLAG (α-FLAG) antibodies in absence (top panels) or presence of EGTA (bottom panels). **d**, Ability of Ca^{2+} to restore PulG levels and pseudopilus formation in WT was assessed using anti-PulG and anti-PulM antibodies. **e**, Pseudopili present on the surface of PAP7460 cells harbouring pCHAP8184 and pCHAP8658 were mechanically sheared and isolated by ultracentrifugation (i). After purification, pseudopili were incubated in buffer alone or buffer supplemented with EGTA or Ca^{2+} for the indicated time and intact pseudopili (p) were separated from the supernatant containing broken or degraded pseudopili (s) by ultracentrifugation. All experiments were repeated three times with reproducible results.


a
G115
G118
G118
G115
S113
S113
S122
D117
E121
F112
D125
I131
I131
D125
N128
Y98
L114
L114
W94HεNε
W129HεNε
A73
A70/
A70
A70
A73/ A73
δ 15N (ppm)
δ 1H (ppm)
b
CSP (ppm)
residue number
K30
D32-V34
V37
D92
W94
S96
D97-Q99
F112
S113-L114
G115
D117
V119
D124 -
G127
I131
G132
c
ΔpulG
M
WT
Ø
PulG
S113A
L114A
D117A
V119A
S122A
D124A
D125A
N128A
W129A
T130A
I131A
G132A
K133A
K134A
Δ128-131
Cells
Pili
PulG
PulG

669

Figure 2. The effect of calcium on PulGp folding and identification of calcium coordinating residues. **a,** Superposed ^{1}H-^{15}N HSQC spectra of 0.5 mM ^{15}N labelled-PulGp purified from the bacterial periplasm (blue contours) in buffer (50 mM HEPES pH 7, 50 mM NaCl), buffer supplemented with 1 mM of calcium (green contours) or buffer supplemented with 20 mM of EGTA (red contours). Some residues exhibiting chemical shift variations are indicated by sequence numbers and by one-letter amino acid code. Insert: zoom showing double peaks in the presence of EGTA for residues A70 and A73. **b**, Histogram showing the chemical shift perturbation (CSP) values of PulGp backbone amide signals (0.5 mM) in the presence of calcium (1 mM) and EGTA (20 mM), as a function of residue numbers. Blue arrows indicate proline residues or amide resonances that could not be unambiguously assigned in the calcium bound state. Red dots indicate residues whose signals were perturbed upon EGTA addition but could not be unambiguously assigned. Residues displaying significant levels of signal perturbations (CSP>0.2 ppm or CSP>0.04 ppm, dashed lines) are labelled. **c,** Bacterial cell and pilus fractions from strains harbouring T2SS (WT) or derivatives lacking *pulG* (*ΔpulG*) and empty vector (Ø) or vector encoding native PulG or its variants with indicated residue substitutions. Equivalent of 0.05 OD_{600nm} of cell and pili fractions were analysed by western blot using anti-PulG antibodies. Molecular mass of standard weight markers (M) is indicated on the left (in kDa). Data shown are representative of three independent experiments.

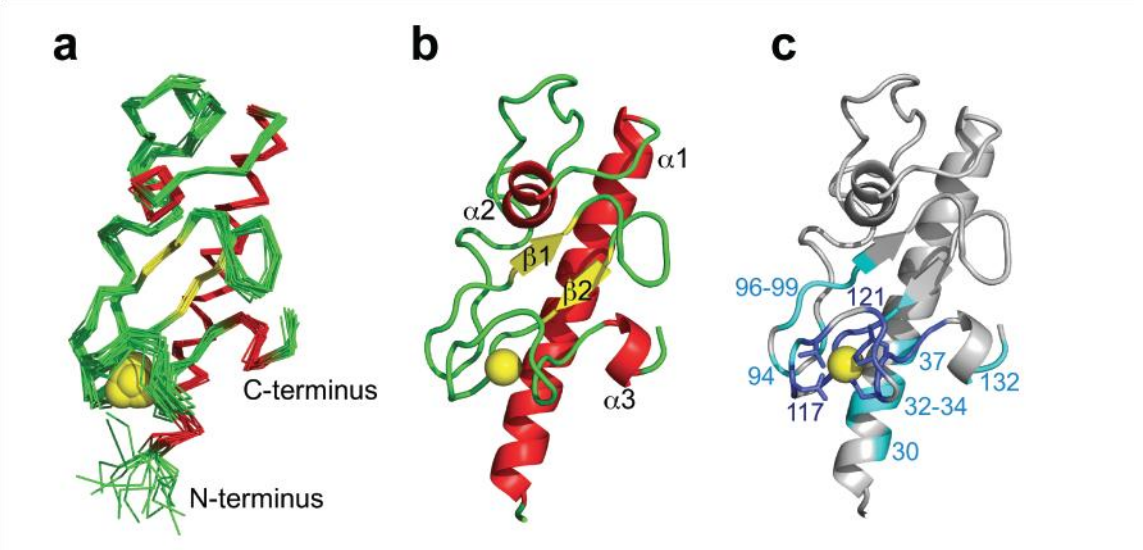


Figure 3. NMR structure of PulGp in the calcium bound state.
a, Superposition of the 15 best-calculated structures. **b**, Ribbon representation of the lowest-energy PulGp conformer. Secondary structure elements are coloured in red (helices) and yellow (β-strands) and calcium atoms are represented as yellow spheres. **c**, Residues that exhibit significant CSP values (above the dashed line threshold in Fig. 2b) are coloured in dark blue (CSP>0.2 ppm) and light blue (CSP>0.04 ppm) in PulGp structure. For clarity, not all significantly affected residues are labelled. Side chains of some of the calcium-coordinating residues are shown as sticks.

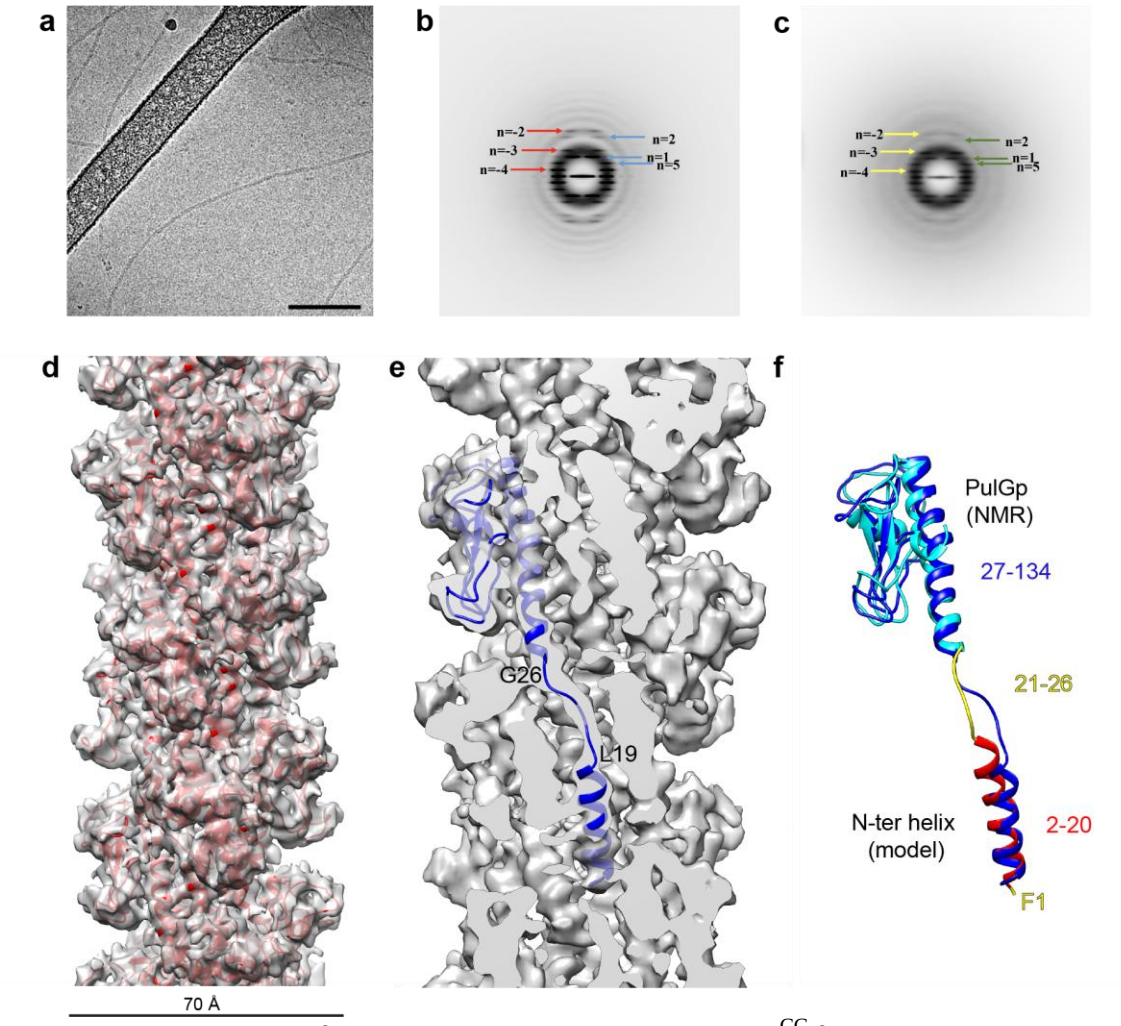


Figure 4. Morphology of *Klebsiella* T2SS pseudopilus PulG^{CC} filament by cryo-EM and reconstruction at ~5 Å resolution. **a**, Representative electron micrograph of *Klebsiella* T2SS pseudopilus PulG^{CC} filament in vitreous ice. Scale bar, 100 nm. Power spectra generated from 72,197 overlapping segments of pseudopilus PulG^{CC} (**b**) and 32,162 overlapping segments of pseudopilus PulG^{WT} (**c**). The layer lines with corresponding Bessel orders are indicated. **d**, An outside view of the cryo-EM reconstruction of PulG^{CC} pilus with the refined atomic model shown in ribbons (red). **e**, Cross-section of the cryo-EM reconstruction with a single PulG^{CC} monomer showing the elongated part (L19-G26) of the N-terminal region and the corresponding density. **f**, Superposition of the initial (cyan/yellow/red) and final (blue) model of a PulG monomer. The PulGp NMR structure (residues 27-134, cyan), excluding flexible M25 and G26, and a model of the N-terminal helix (residues 2-20, red) were docked in the reconstruction and joined by an extended linker (residues 21-26, yellow) before refinement.

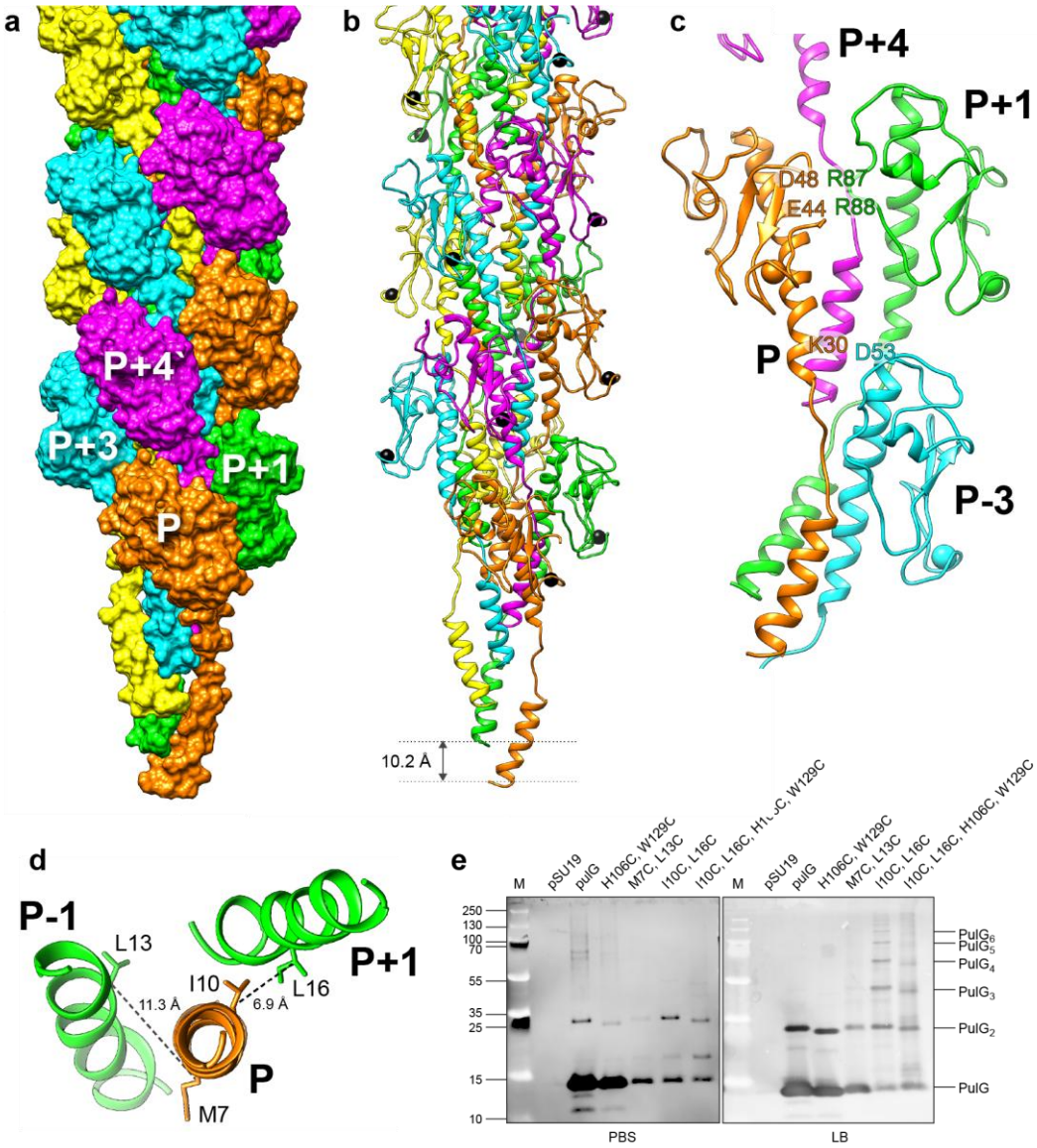


Figure 5. Structure of the PulG^{CC} pilus

a, Surface view of the PulG^{CC} pilus structure where subunits P, P+1, P+2, P+3 and P+4 (along the 1-start helix) are coloured in orange, green, yellow, blue and magenta, respectively. **b**, Ribbon view of PulG^{CC} pilus structure where subunits are coloured as in **a** and calcium ions are shown as black spheres. **c**, Arrangement of neighbouring subunits in the PulG^{CC} structure, showing the location of residues involved in conserved interactions. Calcium ions are shown as spheres. **d**, Top view of the segment F1-L19 of subunits P and P±1 and shortest distances between PulG subunits in the pilus for M7Cβ-L13Cβ and I10Cβ-L16Cβ (dashed lines). **e**, Specific cross-linking of Cys10-Cys16 in PulG^{WT} and PulG^{CC}. Pili were sheared from the cell surface by vortexing and separated from bacteria harbouring plasmid pCHAP8184 (*ΔpulG*) and either empty vector (Ø) or its derivatives encoding PulG variants as indicated above each lane (Supplementary Table 2). Pilus fractions were incubated with agitation in PBS buffer (left) or LB (right) for 1 hr at 30°C. Pili samples were analysed by western blot using PulG antibodies. M, molecular weight markers (in kDa) are indicated on the left. Migration of PulG monomers and oligomers (n=2-6) are indicated on the right. A representative of three independent experiments is shown.